Controlled synthesis of hollow carbon ring incorporated g-C₃N₄ tubes for boosting photocatalytic H₂O₂ production

Hao Luo [a], Tianshang Shan [a], Jianwen Zhou [a], Liulian Huang [a], Lihui Chen [a], Rongjian Sa [b,*], Yusuke Yamauchi [c,d,e,**], Jungmok You [e], Yusuke Asakura [c], Zhanhui Yuan [a,*], He Xiao [a,*]

[a] College of Material Engineering, Fujian Agriculture and Forestry University, Fuzhou, Fujian 350108, China
[b] College of Materials and Chemical Engineering, Minjiang University, Fuzhou 350108, China
[c] Department of Materials Process Engineering, Graduate School of Engineering, Nagoya University, Furo-cho, Chikusa-ku, Nagoya 464-8603, Japan
[d] School of Chemical Engineering and Australian Institute for Bioengineering and Nanotechnology(AIBN), University of Queensland, Brisbane, Queensland 4072, Australia
[e] Department of Plant & Environmental New Resources, College of Life Sciences, Kyung Hee University, 1732 Deogyeong-daero, Giheung-gu, Yongin-si, Gyeonggi-do 17104, South Korea

ARTICLE INFO

ABSTRACT

H₂O₂ production through solar-driven photocatalytic route has received increasing attention. Herein, a carbon ring incorporated hollow g-C₃N₄ tubes (CHCN) was successfully fabricated *via* a novel supramolecular self-assembly strategy, co-inducing by hydrogen bond and covalent bond. The optimum H₂O₂ yield over the CHCN-0.02 reached up to 1.58 mmol L⁻¹ h⁻¹ (AQE= 28.10%, 420 nm), which was 5.4 times significantly higher than that of bulk g-C₃N₄ (0.29 mmol L⁻¹ h⁻¹) under visible light irradiation. Experimental and density functional theory (DFT) calculations revealed that the CHCNs not only expedited the charge carrier transfer/separation but also favored molecular oxygen adsorption and regulated bandgap structure under the in-plane electronic field induced by continuous π-conjugated C_ring, which boosted the ORR efficiency for photocatalytic H₂O₂ synthesis. The optimized CHCN catalyst demonstrated adequate hybrid ORR routes, consisting of a dominated selective one-step two-electron ORR pathway and highly efficient two-step single-electron ORR for H₂O₂ production. Therefore, this work not only provides a new strategy for an efficient H₂O₂ formation using a g-C₃N₄-based photocatalyst but also explores the functionary mechanism of the ORR process and enlightens the way to highly efficient H₂O₂ generation.

1. Introduction

Hydrogen peroxide (H₂O₂), as a green and sustainable chemical, has exhibited extensive applications in pulp bleaching, chemical industry, sewage disposal, and fuel cells [1,2]. Currently, the most widely industrial manufactured technology for H₂O₂ is the anthraquinone oxidation (AO) process, accounting for about 95% of H₂O₂ production in the world [3]. However, the AO process cannot be considered as a sustainable approach because of its intense energy consumption and substantial toxic by-products [4]. Thus, developing a green, low-carbon, and efficient route for H₂O₂ synthesis is urgently demanded.

Photocatalytic H₂O₂ synthesis (PHS) on some semiconductors has received much attention as an alternative solution for industrial AO processes. During the PHS process, molecular oxygen (O₂) and water (H₂O) are commonly regarded as indispensable raw materials and the sunlight is utilized as the driving force, which alleviates the energy dependence on unsustainable fossil fuels and relieves the environmental pressure [5–8]. Briefly, the PHS process can be divided into two-step single-electron oxygen reduction reaction (O₂ + e⁻→•O₂⁻ and •O₂⁻ + 2H⁺ + e⁻→H₂O₂) or one-step two-electron oxygen reduction reaction (O₂ + 2H⁺ + 2e⁻→H₂O₂) [9–11]. It is worth noting that the H₂O₂ formation efficiency is usually limited by the following two aspects: (1) the low conversion rate of •O₂⁻ to H₂O₂ leads to participation of abundant photo-induced electrons only in the one-electron reduction of O₂ to •O₂⁻,

which immensely reduces the utilization of solar energy [12,13]; (2) the slow single-electron oxygen reduction rate ($O_2 + e^- \rightarrow \bullet O_2^-$) is harmful to the formation of superoxide radical and inhibits the H_2O_2 production ($\bullet O_2^- + 2H^+ + e^- \rightarrow H_2O_2$) [14–16]. Consequently, designing a reasonable semiconductor photocatalyst to promote the efficiency for oxygen reduction reaction (ORR) is a desirable strategy to enhance photocatalytic H_2O_2 production.

Graphic carbon nitride (g-C_3N_4), as a metal-free polymeric semiconductor photocatalyst, has recently attracted wide interest in PHS, owing to its high physicochemical stability, low-cost preparation, nontoxicity and unique optical property [17,18]. However, the photocatalytic performance over pristine g-C_3N_4 has been commonly limited by its low specific surface area, rapid charge recombination, insufficient visible-light harvesting, and mediocre surface charge transfer efficiency [19–21]. Fortunately, the modification of g-C_3N_4 is easy to achieve, and able to further optimize its photocatalytic activity. Based on this perspective, a large number of strategies have been explored to boost PHS over g-C_3N_4, such as heterojunction construction [16,22], morphology regulation [23], elemental doping [24–26] and supramolecular self-assembly technology [27–30]. Recently, supramolecular design strategy has been considered as an efficient measurement to introduce certain appointed molecules, chemical functional groups, or targeted elements into the frameworks of g-C_3N_4 at the molecular level, which can internally regulate the band structure in order to improve the photocatalytic activity of g-C_3N_4 [31–33]. Additionally, the supramolecular self-assembly route for g-C_3N_4 fabrication also exhibits large specific surface area providing abundant active sites to enhance the oxygen adsorption and activation on the surface of g-C_3N_4 [34]. However, the reported conventional supramolecular self-assembly strategies for g-C_3N_4 preparation still exhibit the unfavorable transfer and separation efficiency of photo-generated charge carriers, which can be ascribed to the lack of an intrinsic driving force in g-C_3N_4 plane for availably inducing the ordered movement of photo-carriers to appropriate redox sites [35]. According to the previous reports, the π-π stacking interaction between g-C_3N_4 and various kinds of carbon materials, such as carbon dots [33], carbon nanotubes [36] and graphene [37] could effectively intensify the light-harvesting and accelerate the charge separation/transfer rate. However, most of the preparation methods for cavitary g-C_3N_4 were hydrogen bonding-based self-assembly strategy, which gathered plentiful of supramolecular precursors as the first step [27,38]. Moreover, the structure for supramolecular precursors derived from hydrogen bond-driven self-assembling could lead to poor rigidity and stability at high temperature and high pressure [39–43]. Therefore, to address the issue during the hydrogen bonding self-assembly process, the addition of extra covalent bonding on the formation of supramolecular precursors may efficiently regulate the structure of supramolecular precursors [43,44]. Additionally, the derived carbon from covalent precursors can be seamlessly embedded into the basal plane of g-C_3N_4, which is beneficial to the photocarriers separation/transfer for efficient PHS.

In this work, we successfully developed a supramolecular self-assembly technology to synthesize a carbon ring incorporated hollow g-C_3N_4 (CHCN) tubes. Melamine (M)/cyanuric acid (MA) and 1,3,5-Triformylphloroglucinol (TP) served as the precursors. The resulting supramolecular compound was consisted of TP, M, and MA[45]. Due to the collected characterizations, the C_{ring} could be seamlessly embedded into the conjugated network of g-C_3N_4. As a result, the suitable incorporation amount of C_{ring} on the tubular g-C_3N_4 could remarkably optimize the energy band structure, promote the charge carriers' separation/transfer, extend the utilization of visible light, and enhance the adsorption/activation of molecular oxygen to favor oxygen reduction. Notably, the optimal CHCN catalyst possessed a remarkable H_2O_2 evolution activity of 1.58 mmol L^{-1} h^{-1} with a preeminent AQE of 28.1% at 420 nm, which was higher than most of the reported catalysts.

2. Experimental

2.1. Preparation of carbon ring incorporated hollow g-C₃N₄ (CHCN) tubes

First, 5 g of melamine (M) and a certain amount of 1,3,5-Triformylphloroglucinol (TP) were dissolved into 500 mL deionized water under stirring at 80 °C. Then, a certain amount of NaOH solution (1 mmol L^{-1}) was slowly dropped into the melamine solution with a pH of 10 and stirred evenly for 10 min. Second, the suspension was transferred into a Teflon-lined stainless-steel autoclave and thermally treated at 100 °C for 8 h. After cooling down to room temperature, the reddish precipitate was collected and washed with abundant deionized water and then dried at 60 °C overnight. Third, the obtained supramolecular intermediate was put into the tube furnace, heated to 520 °C with a heating rate of 2 °C min^{-1} under argon atmosphere, and then maintained at 520 °C for 1 h. Finally, the collected pale grew solid products were labeled as CHCN-x (where $x = 0.01, 0.02, 0.03$ and 0.06 corresponds to the TP dosage of 0.01, 0.02, 0.03 and 0.06 g, respectively). The corresponding intermediates were named Intermediate-x, where $x = 0.01, 0.02, 0.03$, and 0.06 represent the TP dosage of 0.01 g, 0.02 g, 0.03 g, and 0.06 g, respectively.

2.2. Preparation of bulk g-C₃N₄ (CN)

The CN was prepared by a one-step thermal condensation method. Typically, 2 g melamine (99%, Aladdin) was put into the tube furnace, heated to 520 °C with a heating rate of 2 °C min^{-1} under argon atmosphere, and then maintained at this temperature for 1 h. Finally, the residual yellow solids were obtained, denoted as CN.

2.3. Preparation of hollow g-C₃N₄ (HCN) tubes

The synthesis of HCN was carried out using a process similar to that of CHCN, except for the absence of TP in the reaction mixture. The final light-yellow solid was obtained and labeled as HCN. This sample was also denoted as CHCN-0.00, which signifies that the TP dosage used in the synthesis was 0.00 g. In addition, the corresponding intermediate was named Intermediate-0.00. The more detailed preparation materials and characterizations (theoretical calculations) of all the samples were described in the supporting information.

2.4. Photocatalytic H₂O₂ production

In detail, 50 mg of photocatalyst was dispersed in 50 mL ethanol aqueous solution (10 vol%) and then sonicated for 15 min. The resulting dispersion was vigorously stirred for 30 min in the dark with continuous O_2 blowing to establish the adsorption-desorption equilibrium. Afterward, under continuous oxygen-purging (0.5 L min^{-1}) and stirring (100 rpm), the photocatalyst suspension was irradiated with a 300 W Xe lamp (filter wavelength: λ > 420 nm, the distance between the light source and the suspension surface:10 cm, light intensity: 1.65 Wcm^{-2}). To explore the photocatalytic production trend of H_2O_2, 3 mL suspension was sampled every 1 h and filtrated to remove the photocatalyst. Also, to investigate the decomposition behavior of H_2O_2 on photocatalysts, 50 mg of samples was added to 1 mM H_2O_2 solution (50 mL) with continuous argon purging and stirring for 4 h under visible light irradiation. In every hour, 3 mL suspension was taken out and filtrated. The concentration of H_2O_2 was measured by POD-DPD method according to previous reports [13,46]. Typically, 0.3 mL of phosphate buffer (0.5 M K_2HPO_4 and 0.5 M KH_2PO_4), 30 μL of DPD solution, and 30 μL of peroxidase were mixed with the collected solution. Then, the mixture was shaken for 30 s and detected by UV–vis spectrophotometry at 551 nm. The corresponding cycling tests of the catalysts were carried out under the same condition. The reactive species were analyzed by introducing silver nitrate (AgNO₃, 0.1 mM), p-benzoquinone (PBQ, 0.1
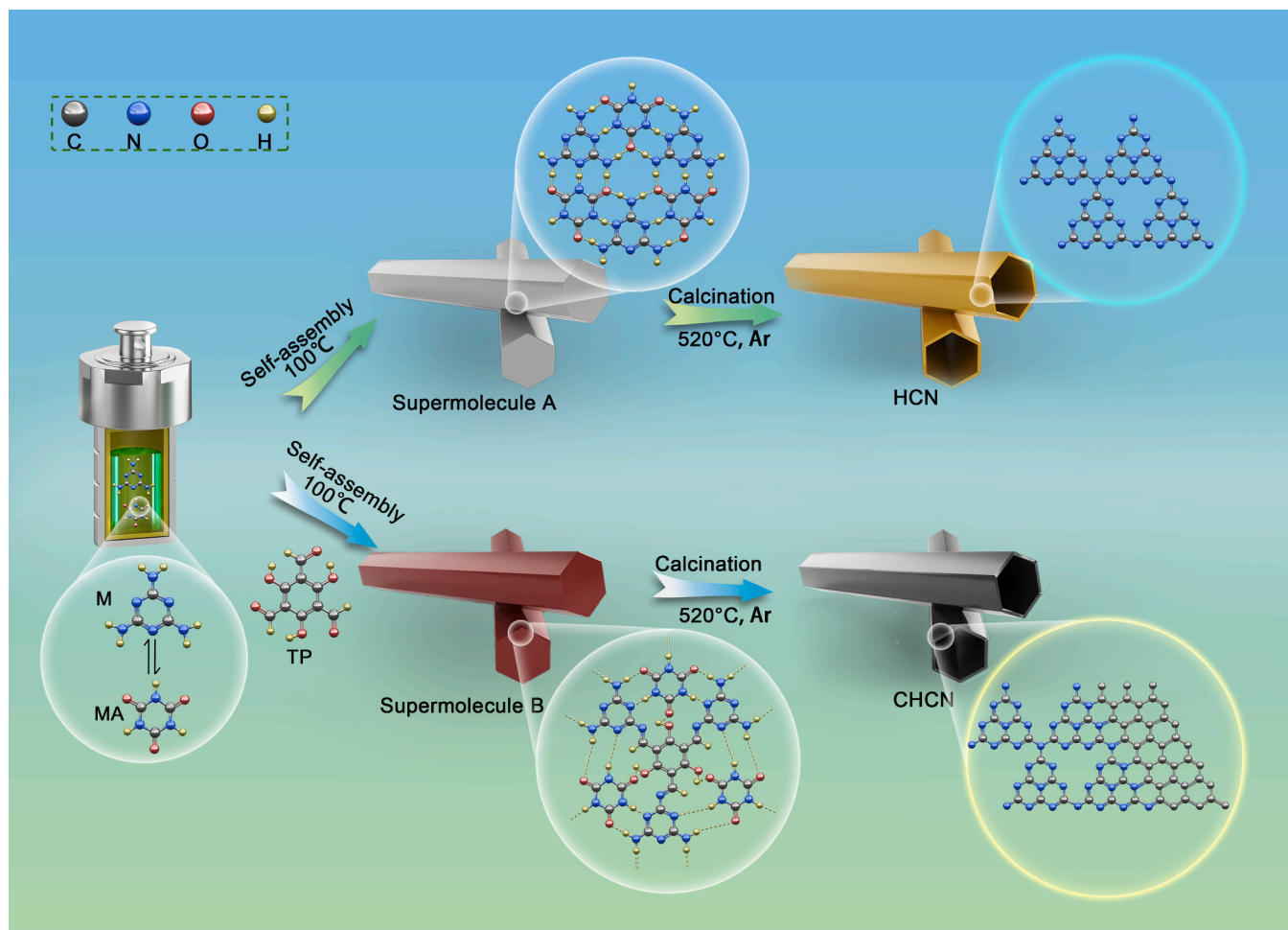
Scheme 1. Presentation of procedures for photocatalysts preparation. Possible structures are also shown within this scheme.

mM), and tert-butyl alcohol (TBA, 0.1 mM) to the suspension for capturing the photo-induced electrons (e⁻), superoxide radicals ($\bullet O_2^-$) and hydroxyl radicals ($\bullet OH$), respectively with pure water as the control.

The apparent quantum efficiency (AQE) of the optimal sample (CHCN-0.02) was detected with different wavelengths (365, 420, 450, 500, 550 nm) irradiation for 1 h. The AQE value was calculated [47] as the following formula (1):

$$AQE = \frac{Number \quad of \quad reacted \quad electrons}{Number \quad of \quad incident \quad photons}$$
$$= \frac{2 \times Number \quad of \quad generated \quad hydrogen \quad peroxide}{Number \quad of \quad incident \quad photons} \quad (1)$$

The efficiency of solar-to-chemical conversion (η) was calculated [48] on the basis of photocatalytic production yields of H_2O_2 by the following Eq. (2):

$$\eta(\%) =$$
$$\frac{[\Delta G \text{for} hydrogen \quad peroxide(kJ/mol)] \times [\text{Formation of} hydrogen \quad peroxide(mol)]}{[Input \quad energy(W)] \times [\text{Reaction times(s)}]}$$
$$\times 100\% \quad (2)$$

where the free energy (ΔG) for H_2O_2 formation was 117 kJ mol⁻¹, the irradiation intensity was 1.65 W cm⁻² measured by a spectroradiometer (CEL-NP2000, China), the irradiation area was 19.625 cm², and the irradiation time was for 1 h.

3. Results and discussion

3.1. Characterization of the prepared photocatalysts

As illustrated in Scheme 1, the C_3N_4 decorated by C_{ring} was synthesized through the supramolecular self-assembly strategy. In this experiment, NaOH solution was used to induce the hydrolysis of melamine (M) and then produce cyanuric acid (MA). Profiting from the abundant oxygen-containing groups of TP, such as hydroxyl and aldehyde groups, ensured that TP was easily combined with M and MA to form the supramolecular precursors. Upon calcination in an argon atmosphere, the C_{ring} derived from TP could be integrally in-situ introduced into the frameworks of g-C_3N_4 (HCN), named as CHCN.

The supramolecular self-assembly results were investigated from the FTIR spectra (Fig. S1a) and XRD patterns (Fig. S1b). In Fig. S1a, the stretching modes of amino group located at 3100–3500 cm⁻¹ confirmed that the planer of supramolecular immediate (Intermediate-0.00 and Intermediate-0.02) was constructed by hydrogen bonding, such as O···H-N and N-H···N, which was in agreement with the previous reports [49, 50]. Moreover, the adsorption band of HCN and CHCN in this range was broader than that of CN and found to be red-shifted [51] (Fig. 1a). The bands observed at 1728 cm⁻¹ and 1775 cm⁻¹ over the intermediates were corresponding to the C═O stretching peaks, and the signals obtained at 1445 cm⁻¹, 763 cm⁻¹, and 1525 cm⁻¹ were the CN--heterocycles stretching peaks, triazine units breathing and stretching peaks, respectively [52] (Fig. S1a). Notably, the intermediate of CHCN-0.02 (Intermediate-0.02) exhibited a lower intensity of the N-H stretching peak and CN-heterocycles peak than that of HCN
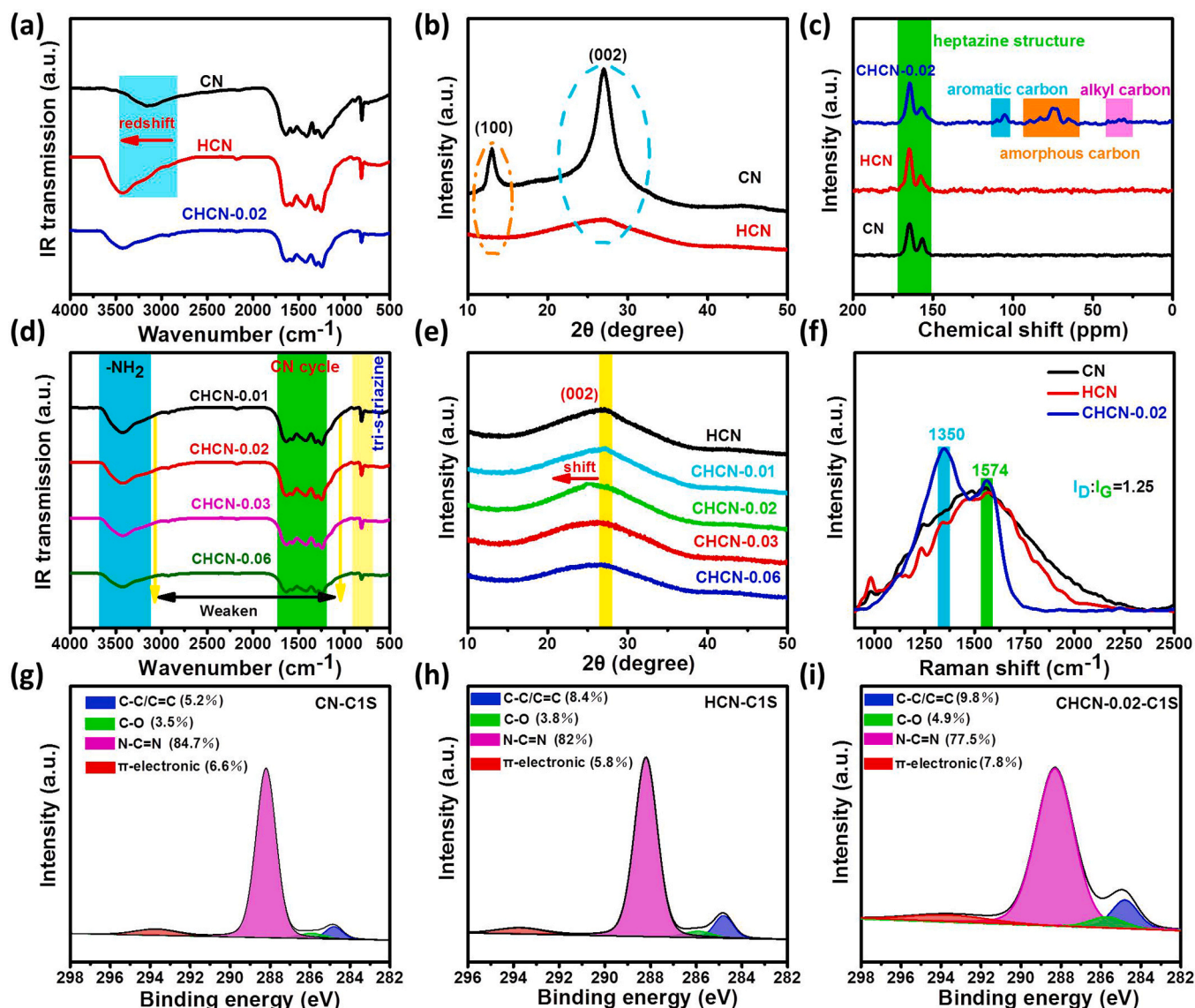
Fig. 1. (a, d) FTIR spectra of CN, HCN, and CHCN-*x* (where *x* = 0.01, 0.02, 0.03, and 0.06 corresponds to the TP dosage of 0.01, 0.02, 0.03, and 0.06 g, respectively), (b,e) X-ray diffraction patterns of CN, HCN and CHCN-*x*, (c) ^{13}C solid-state NMR spectra, (f) Raman spectra, and (g-i) XPS-C1*s* analysis of CN, HCN, and CHCN-0.02.

(Intermediate-0.00) (Fig. S1a), indicating that the TP was involved in forming hydrogen bonds or reacted with the melamine through the Schiff base reaction [53]. Meanwhile, the CHCN displayed a gradual decline in the intensity of the absorption intensity of amino groups (-NH$_2$) with the increase of TP amount (Fig. 1d). The significance of the supramolecular assembly (Intermediate-*x*) process could be further certified by the XRD pattern (Fig. S1b). The diffraction peaks located at about 10.7° and 27.9° corresponded to the periodic arrays of interplanar packing *via* hydrogen bonding and the stacking of layer structure, respectively, indicating the presence of highly hydrogen bonded interaction in supramolecular structure. The peak at 21.7° was also assigned to the (200) planes [54].

In order to investigate the crystal and fingerprint structure of CN, HCN, and CHCN, FTIR and XRD analyses were carried out (Fig. 1b, d, e). As shown in Fig. 1b, the pristine CN directly obtained from melamine by calcination exhibited two obvious characteristic peaks located at 12.8° and 27.2°, which can be well respectively attributed to the (100) and (002) diffraction planes [20]. More precisely, the diffraction peak with (100) at around 12.8° was related to the in-plane ordering of tri-s-triazine units [55], and the diffraction peak with (002) at approximately 27.2° was corresponding to periodic stacking of layers along the

c-axis structures [56,57]. The XRD result of HCN and CHCN showed a significant reduction in the intensity of the (100) diffraction peak, suggesting a disruption in the in-plane ordering of the tri-s-triazine units in the materials [58] (Fig. 1f, e). Moreover, the XRD patterns of HCN and CHCN displayed a less intense diffraction peak at (002) compared to CN, which was in agreement with the characteristic hollow-tube like structure reported previously [49]. In contrast to HCN, the gradual broadening and shifting to lower diffraction angle for diffraction peak with (002) in CHCN with the increase of TP indicated that the carbon ring units could increase the interlayer space (Fig. 1e) [59]. The FT-IR spectra of HCN and CHCN were similar to the pristine g-C$_3$N$_4$ (bulk CN), indicating all the samples possessed the basic molecular structure of g-C$_3$N$_4$ (Fig. 1a). As illustrated in Fig. 1d, the characteristic bands in the regions of 3100–3510 cm^{-1}, 1250–1700 cm^{-1}, and 810–816 cm^{-1} were well associated with the stretching modes of the amino groups (-NH$_2$), the stretching modes of CN heterocycles and the out-of-plane bending of the triazine units, respectively [24]. With an increase of TP, the intensity of these peaks all demonstrated a gradually decreasing trend, due to the formation of coating layer in CN structure caused by C$_{ring}$ [60,61].

To further determine the chemical composition of the CHCN,
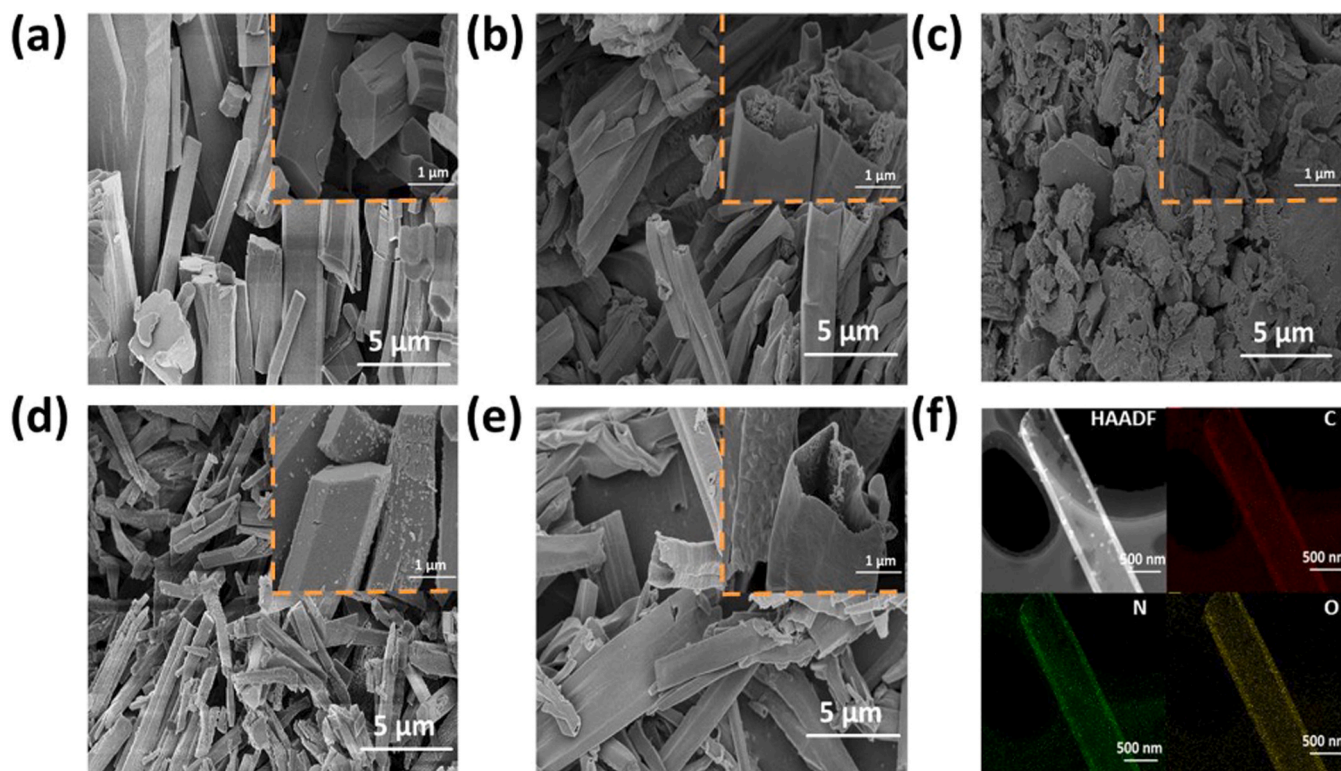
Fig. 2. (a-e) SEM images of (a) intermediate of HCN, (b) HCN, (c) CN, (d) intermediate of CHCN-0.02, and (e) CHCN-0.02. (f) TEM mapping of CHCN-0.02.

^{13}CNMR spectra, Raman spectra, and XPS analyses were used. As shown in Fig. 1c, the ^{13}CNMR spectra of the samples exhibited two obvious characteristic peaks at 157.3 and 165.2 ppm, which confirmed the presence of heptazine structure based on carbon nitride [62]. Different from CN and HCN, the carbon units derived from TP under the calcination process could be observed in CHCN-0.02, where two new peaks located at 105 and 110 ppm were assigned to the aromatic C=C [63]. Meanwhile, the peaks in the range of 61–95 ppm were mainly related to amorphous carbon [51]. In addition, the weak signals obtained at the range of chemical shifts from 30 ppm to 40 ppm were usually attributed to the alkyl carbon.

Raman spectra in Fig. 1f were used to further confirm the presence of C_{ring} incorporated in CN. Well note that there were no characteristic absorption bands observed in CN and HCN, but characteristic features of crystalline graphite bands located at 1350 cm^{-1} (*D* band) and 1575 cm^{-1} (*G* band) could be found in CHCN-0.02 [64]. Typically, the *D* band and *G* band were respectively ascribed to disordered carbon atoms and sp^2-hybridized graphitic carbon atoms, and the intensity ratio of *D* band to *G* band was around 1.25 ($I_D/I_G = 1.25$), although two peaks (D and G bands) are not clearly distinguished [65].

The XPS survey spectra demonstrated that the main element composition of the CN, HCN, and CHCN-0.02 was carbon and nitrogen with a certain amount of oxygen (Fig S2a). As expected in Table S1, the C/N atomic ratio on the surface of CHCN-0.02 (0.605) was higher than that of HCN (0.556) and CN (0.539). To further investigate the origin of increased C element in CHCN-0.02, the high-resolution C 1*s* spectra for the three samples (Fig. 1g-i) could be deconvoluted into four peaks at the binding energy of 284.8, 285.7, 288.2 and 293.6 eV, which were attributed to C-C/C=C, C-O, N-C=N and π electrons, respectively [66]. Significantly, CHCN-0.02 exhibited higher C-C/C=C bonds (9.8%) than CN (5.2%) and HCN (8.4%) (Table S2). The more abundant C element in CHCN-0.02 confirmed the successful incorporation of C_{ring} units into the carbon nitride skeleton. In the N 1*s* spectra, the peaks for sp^2-hybridized aromatic nitrogen (C=N-C), bridging nitrogen (N-(C)$_3$), terminal amino functions (C-NH$_x$) and π electrons =were located at 398.8, 400.1, 401.1

and 404.1 eV, respectively (Fig. S3) [67]. The lower contents of C-NH$_x$ in CHCN-0.02 (10.5%) compared with HCN (11.9%) further proved that the amine function of carbon nitrides was consumed by condensation with TP, which could be also found in FTIR spectra (Fig. 1a, d). Meanwhile, the deconvolution of O 1*s* spectrum of CHCN-0.02 (Fig S2b-d) resulted in two areas at the binding energies of 530.8 and 532.4 eV, corresponding to C-O and absorbed water (H$_2$O), respectively [68]. The above analysis results evidenced the main skeleton of CHCN-0.02 accorded well with that of carbon nitrides, which also confirmed that the C_{ring} conjugated with the main framework of carbon nitrides *via* continuous π- conjugated bonds.

As illustrated in Fig. 2a, d, the supramolecular intermediates of HCN and CHCN-0.02 (*i.e.*, Intermediate-0.00 and Intermediate-0.02) demonstrated a solid column morphology. After the further thermal polymerization of the supramolecular intermediate, the obtained HCN and CHCN-0.02 exhibited an open hollow nanotube morphology with the diameter of 0.5–2.5 μm (Fig. 2b, e). The morphology of the original CN, produced through direct calcination of melamine, was predominantly comprised of irregularly stacked masses with a broad size range (Fig. 2c). Therefore, the self-assembly strategy had a significant influence on the morphology control of g-C$_3$N$_4$. Fig. 2f displays the elemental mapping images of CHCN-0.02, which revealed the uniform distribution of three elements (C, N and O) across the entire nanotube, consistent with the XPS result.

From the TG curves of the supramolecular intermediates of HCN and CHCN-0.02 (*i.e.*, Intermediate-0.00 and Intermediate-0.02) under an argon atmosphere with a heating range of 30–800 °C (Fig. S4a), the rapid thermal decomposition of supramolecular intermediate occurred at the range of 320–420 °C, which could be ascribed to its unstable structure consisted with hydrogen bonding. This result revealed the transformation process of supramolecular intermediate to hollow-tube structure. The thermal decomposition of the intermediates of HCN and CHCN-0.02 was completed at approximately 600 °C. To make a comparison, we also studied both HCN and CHCN-0.02. At around 600 °C, the HCN underwent complete decomposition, while the CHCN-0.02 left
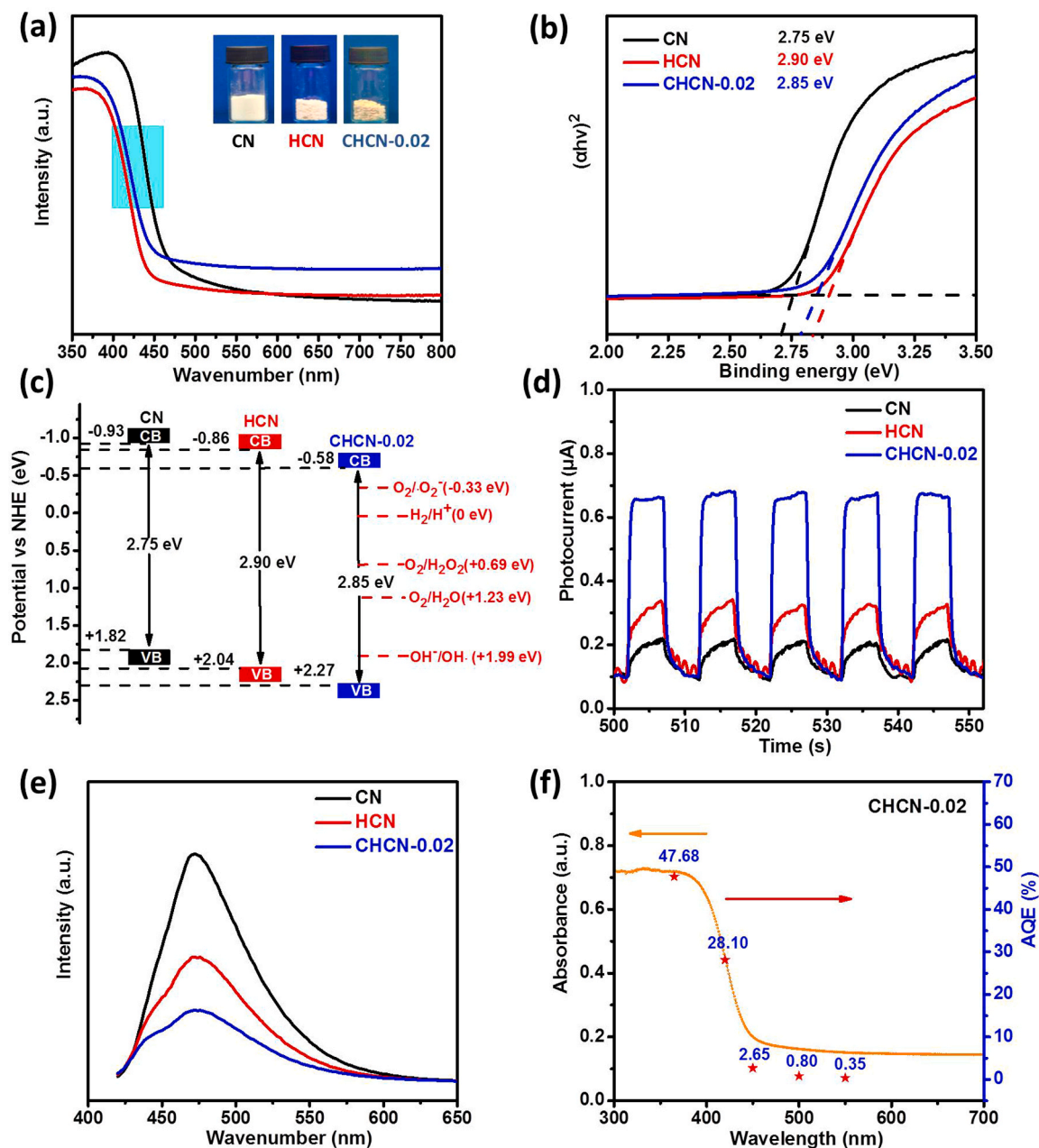
Fig. 3. a) UV–vis DRS spectra, b) Tauc plots, c) energy band structures, d) Transient photocurrent response curves, e) photoluminescence spectra of CN, HCN, and CHCN-0.02, and f) Wavelength-dependent apparent quantum efficiency of CHCN-0.02 on H_2O_2 production reaction.

behind about 15 wt% of residue, which was likely due to the presence of crystalline carbon originating from TP (Fig. S4b). Furthermore, the HRTEM image revealed the presence of highly graphitized regions in certain areas [69], while the amorphous regions were likely attributed to the disordered structure of carbon nitride (Fig. S5). As expected, the BET surface area of the tubular CHCN-0.02 and HCN were clearly larger than that of bulk CN. After calculation, the specific surface areas of the three samples were 72.99 m^2 g^{-1}, 54.42 m^2 g^{-1}, and 7.51 m^2 g^{-1}, respectively.

The optical property and electronic band structure of the photocatalysts were investigated *via* UV–vis spectra, valance band XPS spectra (VB-XPS), and Mott–Schottky plots (M-S plots). As illustrated in Fig. 3a, HCN and CHCN-0.02 exhibited an apparent blue shift in their absorption edge compared with the CN, which was attributed to the strong quantum confinement effect induced by their porous tubular structure [70]. Meanwhile, the absorption spectra of CHCN-0.02 demonstrated an

obvious redshift with respect to HCN, indicating the more efficient visible light harvest promoted by the incorporated C_{ring}. More significantly, the visible light response intensity of CHCN-0.02 was strengthened, which could be ascribed to the extended π-electron delocalization that arises from the conjugative effect between the C_{ring} and g-C_3N_4 [71]. The bandgaps of the samples were calculated according to the Kubelka-Munk function: $\alpha h\nu = A(h\nu - E_g)^r$ (where E_g: band gap, α: absorption coefficient, h: Plank's constant, ν: light constant, A: proportionality constant, and the value of $r = 2$ due to the direct band gap material for g-C_3N_4). Correspondingly, the E_g values of the CN, HCN, and CHCN-0.02 were determined as 2.75, 2.90, and 2.85 eV, respectively (Fig. 3b). Meanwhile, the band levels of the samples were further measured by M-S plots and VB-XPS spectra. The flat band potential (E_{fb}) of CN, HCN, and CHCN-0.02 were calculated to be − 0.24, − 0.37 and − 0.35 eV (*vs.* Ag/AgCl) from M-S plots (Fig. S6a-c), and the positive slopes indicated that these photocatalysts belong to the typical *n*-type
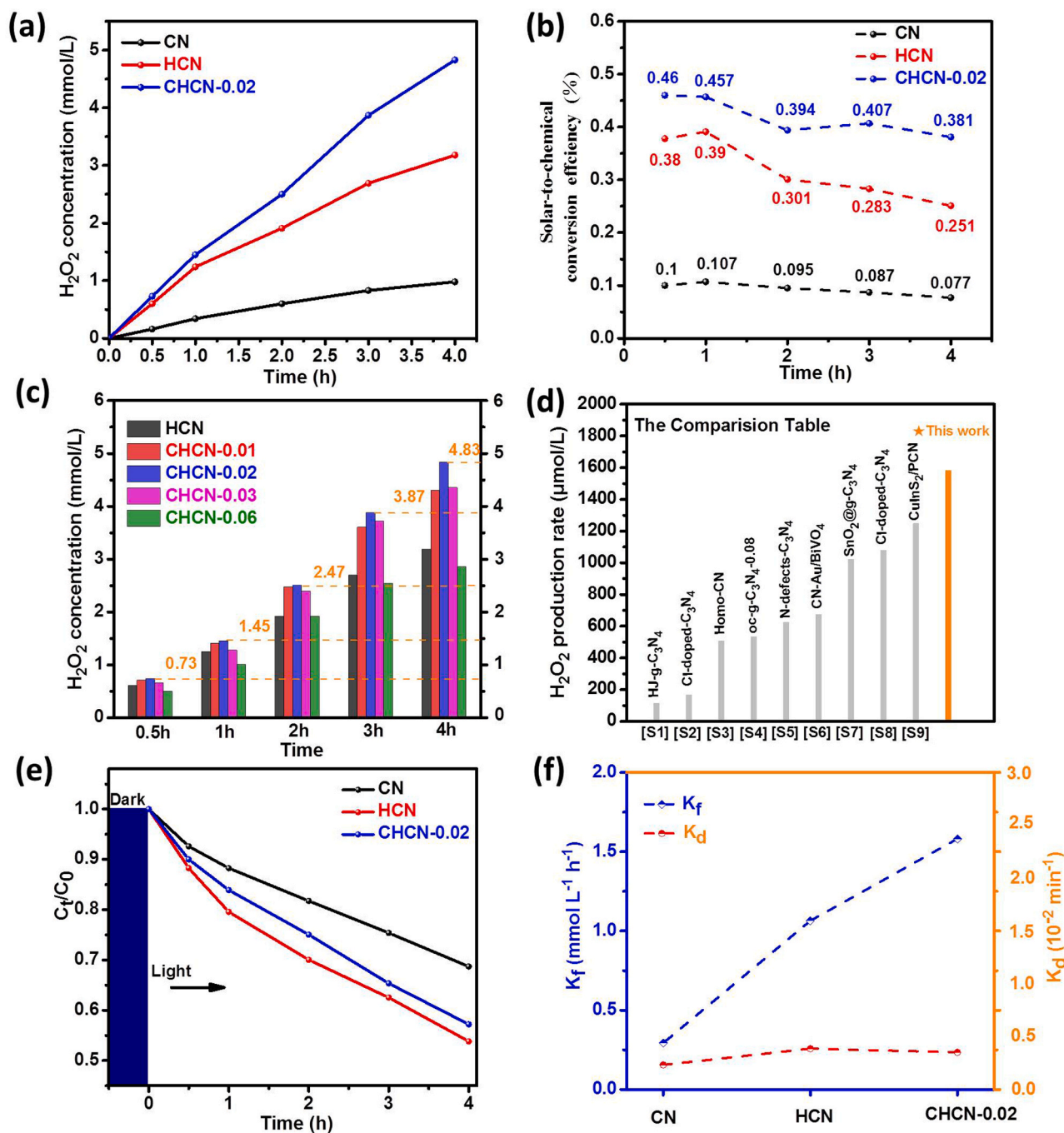
Fig. 4. a) Photocatalytic production of H_2O_2 over CN, HCN, and CHCN-0.02 under visible light irradiation, b) The solar-to-chemical conversion efficiency (SCC) of the different photocatalysts, c) Photocatalytic H_2O_2 production on CHCN-x (where x represents the usage amount of TP, served as 0 g, 0.01 g, 0.02 g, 0.03 g, and 0.06 g.), d) Comparison for H_2O_2 production with other photocatalysts in recent reports, e) Photocatalytic decomposition behavior of H_2O_2 under visible light irradiation and argon atmosphere, f) Fitted formation rate (K_f) and decomposition rate values (K_d) for H_2O_2 photocatalytic production.

characteristic semiconductor [72]. The binding energy of the valence band photoelectrons estimated from VB-XPS spectra (Fig. S6d) for CN, HCN, and CHCN-0.02 were $+1.86$ eV, $+2.21$ eV, and $+2.42$ eV, respectively. Thus, the valence band positions ($E_{VB}= E_{XPS-VB}+E_{fb}+E_{Ag/AgCl}^\theta$, $E_{Ag/AgCl}^\theta=0.2$ eV) of the CN, HCN, and CHCN-0.02 were determined as $+1.82$ eV, $+2.04$ eV, and $+2.27$ eV, respectively. Meanwhile, the correlative conduction band positions (E_{CB}) were -0.93 eV, -0.86 eV, and -0.58 eV, calculated by the formula: $E_{CB}= E_{VB}-E_g$ [73]. In conclusion, the energy band structures of the three samples are described in Fig. 3c. As a result, the three samples all possessed a more negative reduction potential than that of O_2/H_2O_2

($+0.69$ eV *vs.* NHE) [15], although the CB potential of the CHCN-0.02 shifted to a more positive potential with respect to CN or HCN. However, it's worth noting that the CHCN-0.02 exhibited the deepest position of VB, which indicated that it possessed the strongest ability to generate more O_2 and protons from ethanol oxidation.

Apart from the effect on the bandgap structure and morphology of g-C_3N_4, carbon ring units embedded into the molecular structure of g-C_3N_4 can also improve the separation/transfer of photo-generated carriers, which were investigated by the photoluminescence (PL) spectra, photocurrent measurement, and electrochemical impedance spectroscopy (EIS). Fig. 3e exhibited that the PL intensity of CHCN-0.02 was
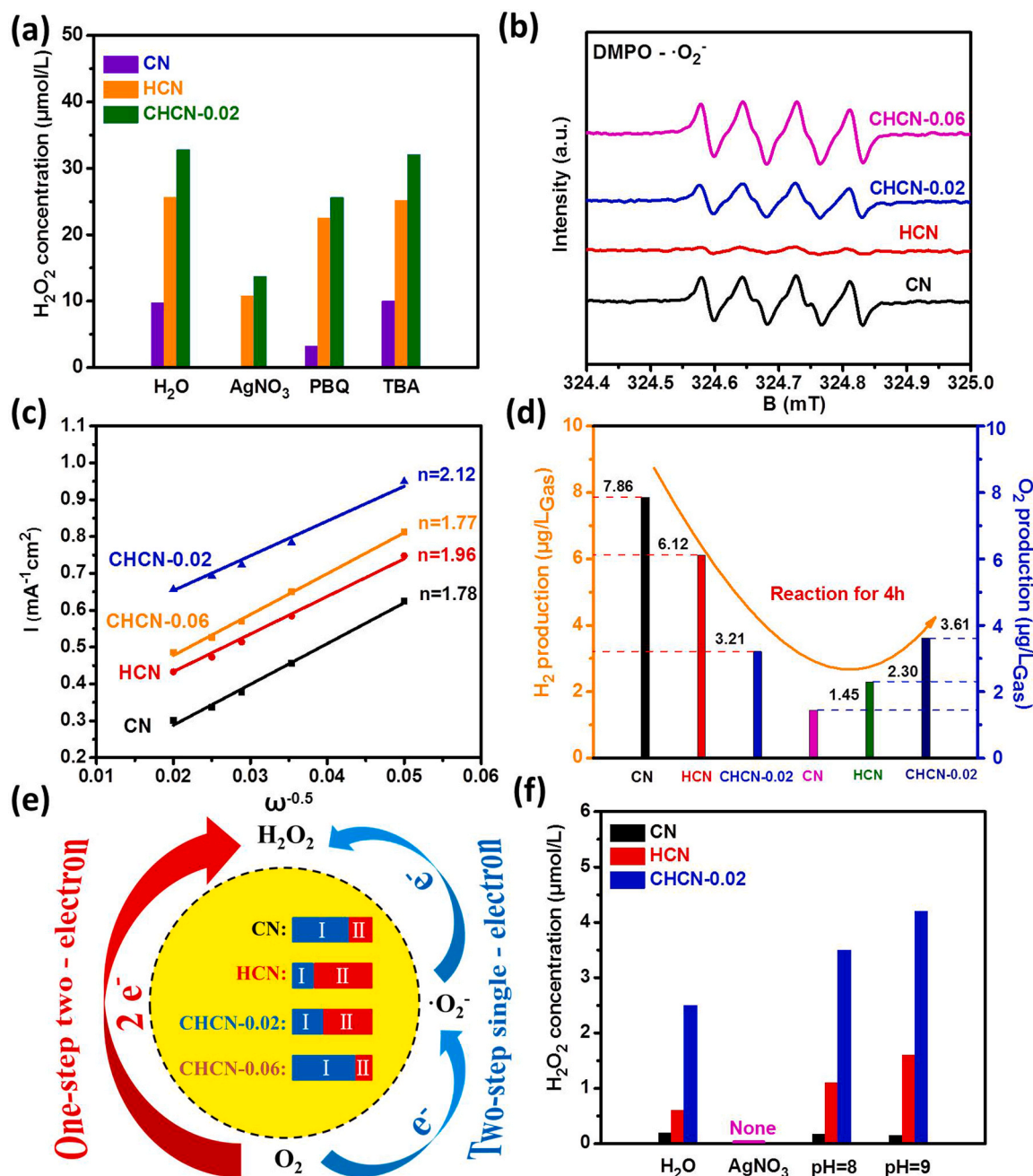
Fig. 5. a) The influence of scavengers (0.1 mM AgNO$_3$, PBQ,TBA solutions for e$^-$, •O$_2$, •OH, respectively) on photocatalytic H$_2$O$_2$ production (condition: reaction time 1 h; O$_2$ atmosphere) over the CN, HCN, and CHCN-0.02, using H$_2$O as the control, b) Electron paramagnetic resonance spectra of the DMPO-•O$_2$ adduct for CN, HCN,CHCN-0.02, and CHCN-0.06, c) The Koutecky-Levich (K-L) plots of CN, HCN, CHCN-0.02 and CHCN-0.06, d)The photocatalytic hydrogen evolution and oxygen capacity of CN, HCN, and CHCN-0.02 under the visible light irradiation for 4 h, e) Proposedmechanism for photocatalytic H$_2$O$_2$ production, f) Comparison of CN, HCN, and CHCN-0.02 for different conditions of photocatalytic H$_2$O$_2$ production under the Ar atmosphere (reaction time 1 h; 0.1 mM AgNO$_3$ solution; NaOH solution: pH=8, pH=9; using H$_2$O as the control).

obviously the lowest, and the order of the PL intensity was presented as the following: I$_{CHCN-0.02}$ <I$_{HCN}$<I$_{CN}$, proving that the recombination efficiency of photo-generated electron-hole pairscan be effectively inhibited by the hollow tubular structure and incorporation of C$_{ring}$ [31, 35]. Meanwhile, the photocurrent responses curves and EIS spectra were collected for CN, HCN, and CHCN-0.02 electrodes to further explore the charge separation/transfer process. In accordance with the expectation, the arc radius of the HCN and CHCN-0.02 were all smaller than that of CN, and the CHCN-0.02 exhibited the smallest arc radius, which indicated that the CHCN-0.02 possessed the smallest resistance, or the strongest ability for photocarriers transfer (Fig. S7). Correspondingly,

this similar trend can be also observed in photocurrent measurement. From the photocurrent measurement illustrated in Fig. 3d, the photocurrent intensity of the CHCN-0.02 was the highest among all the samples, further implying that the in-plane incorporated C$_{ring}$ can efficiently promote the charge separation and transfer rate of CHCN-0.02. The trend of the apparent quantum efficiency (AQE) curve on H$_2$O$_2$ production over CHCN-0.02 accorded well with its UV–vis absorption spectra, and the value of AQE was found to be decreased with the increasing wavelengths (Fig. 3f). Typically, the AQE of H$_2$O$_2$ production was measured with different light wavelengths including 365, 420, 450, 500 and 550 nm for 1 h irradiation, and the corresponding H$_2$O$_2$

production was 1967 µmol L^{-1}, 2530 µmol L^{-1}, 264.09 µmol L^{-1}, 98.33 µmol L^{-1}, and 47.56 µmol L^{-1}, respectively (Fig. S8). As the calculated results, the CHCN-0.02 demonstrated a remarkable AQE up to 47.78% at 365 nm, 28.10% at 420 nm, and even the AQE value can also achieve 2.65%, 0.80%, and 0.35% at longer visible light wavelength of 450, 500 and 550 nm, respectively.

3.2. Photocatalytic H_2O_2 production

As illustrated in Fig. 4a, the photocatalytic H_2O_2 generation from the samples were investigated under four-hour visible light irradiation (λ > 420 nm) (It is noted that the standard curve and equation of H_2O_2 concentration are shown in Fig. S9.). Obviously, the 1D tubular HCN exhibited excellent H_2O_2 production with 3.11 mmol L^{-1}, exceeding that of bulk CN (0.998 mmol L^{-1}) by 2.12 times. The improvement of the photocatalytic performance was ascribed to the hollow tubular structure of HCN, leading to abundant active sites and rapid separation/ transfer of photo-generated electron/hole pairs, which was in line with the results of electrochemical characterization and PL spectra (Fig. 3d, e, Fig. S7). Besides, compared with HCN, when the C$_{ring}$ was incorporated into the molecular structure of g-C$_3$N$_4$, the H_2O_2 evolution for CHCN-0.02 was further up to 4.83 mmol L^{-1} due to the extra intrinsic driving force induced by the C$_{ring}$, resulting in faster intermolecular charge transferring. Correlatively, after 4 h photoreaction, the solar-to-chemical conversion efficiency of CHCN-0.02 reached as high as 0.381%, which was 4.9 times of the CN (0.077%) and 1.52 times of the HCN (0.251%) (Fig. 4b). Noting that, the photocatalytic activity of CHCN was influenced by the introduction value of C$_{ring}$ derived from TP (Fig. 4c) and the most appropriate usage amount of TP (0.02 g) was about 20 wt% of the g-C$_3$N$_4$, which was in agreement with the TG analysis (Fig S4b).
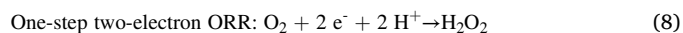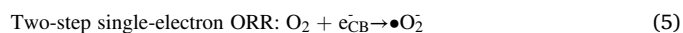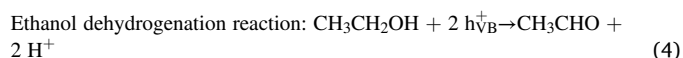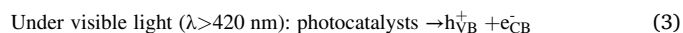
The decomposition behaviors of H_2O_2 on photocatalysts were explored under the visible light irradiation and argon atmosphere with 1 mmol L^{-1} H_2O_2 solution. Significantly, the H_2O_2 decomposition level of HCN and CHCN-0.02 was respectively ~46% and ~43%, which was higher than that of CN with ~31% after 4 h light illumination (Fig. 4e). These results could be ascribed to the extremely larger specific surface area of the HCN and CHCN with respect to CN, leading to more H_2O_2 molecules absorbing on the surface of catalysts and decomposing into •O$_2^-$ or •OH by the photo-generated holes/electrons [74]. Hence, the photocatalytic H_2O_2 production was the outcome of the dynamic process between the formation and decomposition of H_2O_2. The H_2O_2 decomposition (K_d) and formation kinetics (K_f) were calculated with the following formula: $[H_2O_2]=K_f / K_d\times [1-exp(-K_dt)]$, where t represents the photoreaction time, $[H_2O_2]$ is the concentration of the H_2O_2 production (mmol L^{-1}) [75]. As illustrated in Fig. 4f, the K_d of HCN (0.002567 min^{-1}) and CHCN-0.02 (0.002342 min^{-1}) was higher than that of CN (0.001546 min^{-1}), but the K$_f$ value of CN(0.2933 mmol^{-1} L^{-1} h^{-1}) was much lower than that of HCN (1.0644 mmol^{-1} L^{-1} h^{-1}) and CHCN-0.02 (1.5816 mmol^{-1} L^{-1} h^{-1}). Therefore, the CHCN-0.02 exhibited the excellent ability of photocatalytic H_2O_2 generation, which was higher than those of most current reports (Fig. 4d, Table S3).

Moreover, cycling tests were used to evaluate the photo-stability of the as-prepared samples (Figs. S10, S11). After three cycles of measurement, the photocatalytic activity of the three photocatalysts was almost unchanged. As illustrated in Fig. S10, the FTIR spectra exhibited that the characteristic peaks of both the fresh and reused CHCN-0.02 catalysts were nearly unchanged, further confirming the superior stability of the CHCN-0.02 during the photoreaction.

3.3. Mechanism of photocatalytic H_2O_2 production

In general, there are two main pathways for photocatalytic H_2O_2 production consisting of two-step single-electron oxygen reduction reaction (ORR) and one-step two-electron ORR. In this work, ethanol was used as the proton donor, and oxygen as the reduced raw material.

Typically, the process of photocatalytic H_2O_2 production was illustrated as the following (3−8):

Under visible light (λ>420 nm): photocatalysts →h$_{VB}^+$ +e$_{CB}^-$ (3)

Ethanol dehydrogenation reaction: $CH_3CH_2OH + 2 h_{VB}^+ \rightarrow CH_3CHO + 2 H^+$ (4)

Two-step single-electron ORR: $O_2 + e_{CB}^- \rightarrow \bullet O_2^-$ (5)

$\bullet O_2^- + H^+ \rightarrow HO_2$ (6)

$HO_2\bullet + H^+ + e_{CB}^- \rightarrow H_2O_2$ (7)

One-step two-electron ORR: $O_2 + 2 e^- + 2 H^+ \rightarrow H_2O_2$ (8)

As shown in Fig. 5a, the active species eliminating experiments were carried out under the pure O_2 atmosphere for 1 h visible light irradiation to investigate the ORR pathway over the CN, HCN and CHCN-0.02. In these experiments, silver nitrate (AgNO$_3$), p-benzoquinone (PBQ), and tert-butylalcohol (TBA) solutions were used as the trapping agents of e$^-$, •O$_2^-$ and •OH, respectively, and the pure water was used as the control [10]. Clearly, the photocatalytic H_2O_2 production of the three samples exhibited a dramatically decreasing trend in AgNO$_3$ system compared with the pure H_2O system. There was no H_2O_2 generation over CN, suggesting that the photo-generated electrons were highly crucial for the ORR process. Meanwhile, with the addition of PBQ obviously inhibited the H_2O_2 generation around 67% of decrease over CN, implying that •O$_2^-$ had a significant effect on the CN system and confirming the photocatalytic H_2O_2 production over the CN was mainly through the two-step single-electron ORR. However, the slightly depressed degree of H_2O_2 production observed in HCN (12%) and CHCN-0.02 system (23%) was the evidence of 2e$^-$ ORR process occurred on HCN and CHCN-0.02 mainly dominated by the direct one-step two-electron ORR [6]. Besides, the deep inhibiting effect on H_2O_2 evolution over the CHCN-0.06 (70%) can be also observed in the PBQ system (Fig. S12), which was the typical characteristic for the two-step single-electron ORR. Thus, it was clear that the •O$_2^-$ generation was easily improved with the increase of C$_{ring}$ loading and then further enhanced the effect of two-step single-electron ORR during photocatalytic H_2O_2 synthesis.

In order to further confirm the inference for ORR pathway, the •O$_2^-$ was detected by the electron paramagnetic resonance (EPR) technique. Fig. 5b demonstrates the EPR signals of the four samples using DMPO as the trapping agent for ·O$_2^-$ radical species [38]. Obviously, the obtained ·O$_2^-$ signal intensities of the HCN and CHCN-0.02 were weaker than that of CN, and the HCN exhibited the weakest signal intensity of ·O$_2^-$ radical species, indicating that the least ·O$_2^-$ radical species generated over HCN under visible light irradiation. Also, it can be clearly observed that CHCN-0.06 presented the highest intensity of EPR signals among all the samples. Moreover, the linear sweep voltammetry (LSV) curves of CN, HCN, CHCN-0.02, and CHCN-0.06 were measured on a rotating disk electrode (RDE) with different speeds of 0, 400, 800, 1200, 1600, and 2500 rpm to further investigate the ORR pathway for H_2O_2 generation (Fig. S13). The corresponding average number of transfer electrons (n value) was calculated with the following Koutecky-Levich (K-L) equation: $J^{-1} = J_L^{-1} + J_K^{-1}$ (where J: limiting current, J$_L$: Levich current and J$_K$: kinetic current) [13]. As a result, the n values of CN, HCN, CHCN-0.02, and CHCN-0.06 determined from the K-L plots were 1.78, 1.96, 2.12, and 1.77, respectively (Fig. 5c), which implied that HCN and CHCN-0.02 possessed more one-step two-electron ORR process for the H_2O_2 evolution than that of CN and CHCN-0.06, because the theoretical n value was close to 2 [76]. Besides, the ORR process of H_2O_2 generation also competes with the hydrogen (H$_2$) evolution reaction [9]. After 4 h visible light irradiation under the vacuum conditions, the photocatalytic H$_2$ evolution of CN, HCN, and CHCN-0.02 exhibited 7.86 µg L$_{gas}^{-1}$, 6.12 µg L$_{gas}^{-1}$, and 3.21 µg L$_{gas}^{-1}$, respectively, and the correlative O_2 presented as the following order: CN<HCN<CHCN-0.02, which indicated the most efficient ORR for CHCN-0.02 among the three samples
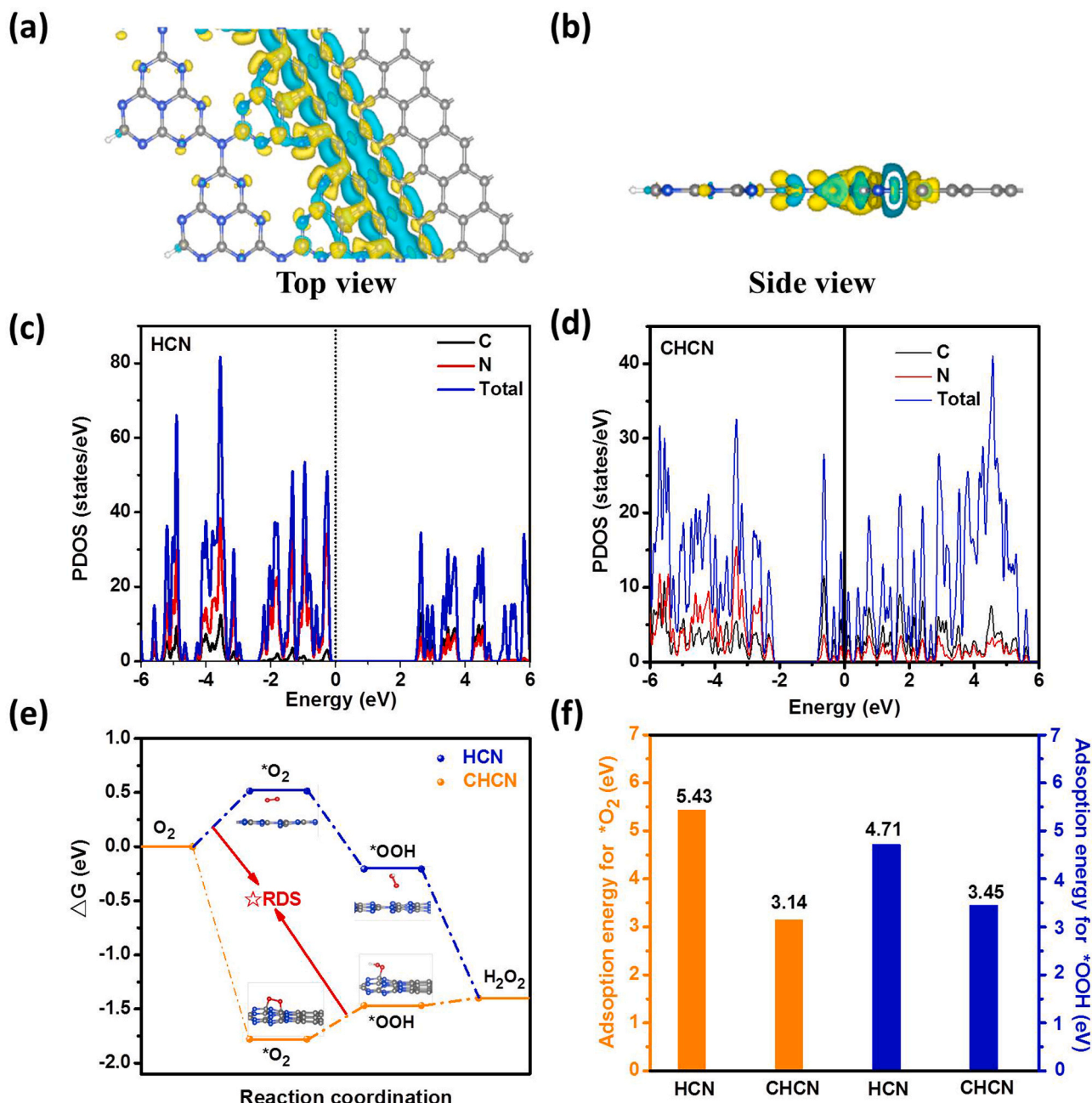
Fig. 6. a,b) Differential charge of CHCN from the top view and side view, c,d) Calculated DOSs for HCN and CHCN, e) Free energy diagrams of ORR steps for HCN and CHCN, f) The adsorption energy for *O_2/*OOH on HCN and CHCN.

(Fig. 5d).

Based on the above results, the superior photocatalytic performance for H_2O_2 production over the CHCN-0.02 could be mainly attributed to the following aspects: (1) The 1D tubular structure of g-C_3N_4 exhibited a dominated direct one-step $2e^-$ ORR process, which can provide the high selective $2e^-$ ORR route for the H_2O_2 evolution; (2) The in-plane C_{ring} based on the g-C_3N_4 was beneficial to the reduction of O_2 to $\cdot O_2^-$ and the suitable amount of C_{ring} can efficiently achieve the conversion of $\cdot O_2^-$ to H_2O_2. However, the excess composite amount of C_{ring} would induce the superfluous $\cdot O_2^-$ radical species produced and lead to a low conversion efficiency of $\cdot O_2^-$ to H_2O_2. As a result, the ORR process for H_2O_2 generation over the CN, HCN, CHCN-0.02, and CHCN-0.06 could be described in Fig. 5e.

Concerning the H_2O_2 generation from water oxidation reaction (WOR), the $\bullet$OH was also tested on EPR measurement (Fig. S14). As a

result, the $\bullet$OH was observed in all the samples under the visible light irradiation, and the intensities of the three samples were listed as the following order: $I_{CN} < I_{HCN} < I_{CHCN-0.02}$, indicating that the $\bullet$OH could be generated over the catalysts during the photoreaction. Differently from the CN (+1.82 eV), the VB level of the HCN (+2.04 eV) and CHCN-0.02 (+2.27 eV) were more positive than the oxidation potential of $OH^-/\bullet OH$ (+1.99 eV vs. NHE) [74]. Therefore, the emergence of the $\bullet$OH over the CN was mainly *via* the decomposition of H_2O_2 ($H_2O_2 + e_{CB}^- \rightarrow \bullet OH + ^-OH$) [77]. After adding the TBA as the trapping agent of $\bullet$OH (Fig. 5a), the H_2O_2 production of the CN was almost not to be changed, but the slight depression of the H_2O_2 production could be observed in HCN (0.5%) and CHCN-0.02 (1.2%), implying the weak effect of the WOR process on H_2O_2 production. To further explore the influence of WOR process on H_2O_2 production, the photocatalytic H_2O_2 production over the catalysts was employed under the Ar atmosphere for 1 h visible light
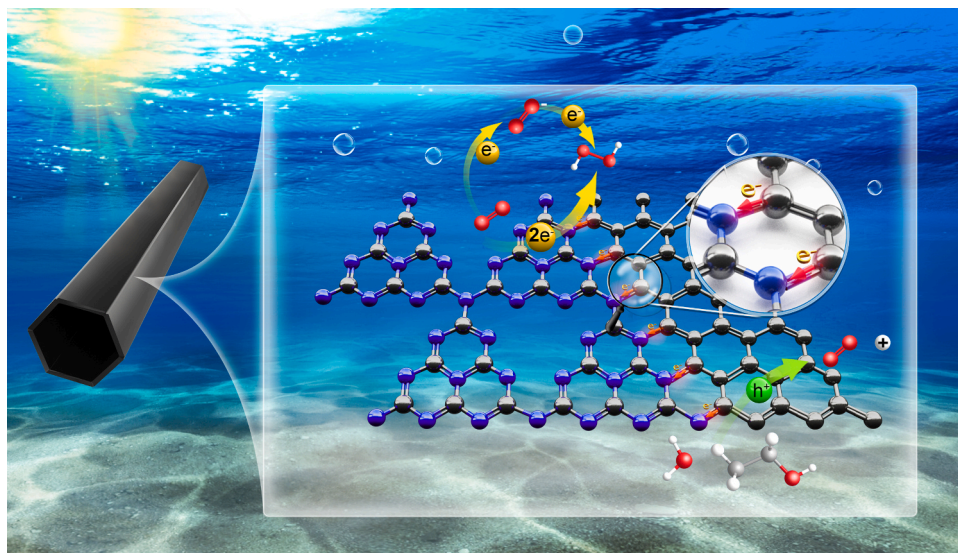
Scheme 2. The proposed mechanism for photocatalytic H_2O_2 production over the CHCN-0.02.

irradiation (Fig. 5f). Interestingly, the H_2O_2 generation over the samples was scarcely observed in $AgNO_3$ system. Meanwhile, there were only about 0.25 μmol L^{-1}, 0.53 μmol L^{-1} and 2.51 μmol L^{-1} H_2O_2 production obtained over the CN, HCN, and CHCN-0.02 in the pure water system. In addition, compared to the H_2O system, it can be observed that the increasing production of H_2O_2 performed over HCN and CHCN-0.02 under weakly alkaline conditions (pH=8 and 9), which was ascribed to the more conversion of OH^- to •OH, resulting in more H_2O_2 generation ($2•OH \rightarrow H_2O_2$) [78]. These results further revealed the importance of photo-generated electrons and molecular oxygen during the ORR process, but confirmed that the WOR played a minor role in photocatalytic H_2O_2 production.

To further investigate the ORR process on the photocatalytic H_2O_2 generation, density functional theory (DFT) calculations were conducted. The charge density distributed between the framework of g-C_3N_4 and the C_{rings} in the structure of CHCN was illustrated in Fig. 6a, b. It can be found that the area of blue cloud (electron-donor regions) and yellow cloud (electron-acceptor regions) were respectively located at the C_{rings} and the basal plane of g-C_3N_4, which indicated that the electrons tended to transport from the C_{rings} to g-C_3N_4. Meanwhile, the results of frontier molecular orbital distribution for CHCN (Fig. S15c, d) can further confirm the intermolecular charge transfer channels between the C_{rings} and g-C_3N_4. Obviously, the HOMO and LUMO of CHCN were located on the C_{rings} and g-C_3N_4, respectively, which was the characteristics of built-in donor–acceptor system [79–81]. These DFT calculated results were in agreement with the data analysis of photocurrent measurement, PL, and EIS spectra (Fig. 3d, e, Fig. S7), further demonstrating that the embedding of C_{rings} into the basal plane of g-C_3N_4 can efficiently induce an intermolecular driving force to promote the charge carriers transfer/separation.

In addition, the energy band structure of HCN and CHCN can be performed on the electron densities of states (DOS). As illustrated in Fig. 6c, the DOS result for HCN met well with the semiconductor character. Typically, there was not any electron distribution around the Fermi level for HCN, and its calculated Humo-Lumo gap (Figs. S15a, b) was 2.44 eV. Conversely, for CHCN, there were a large number of mobile electrons around its Fermi level, and the Fermi level was across to the state of band gap, which was attributed to the new intermediate state introduced by C_{rings}. Meanwhile, it was clear that the new intermediate state was above its valence band and according well with the energy band structure analysis obtained from the UV–vis DRS spectra, M-S plots, and VB-XPS results (Fig. 3a, Fig. S6). Therefore, compared with the HCN, the position of the conduction band for CHCN exhibited a

positive shift, and the band gap became narrower, which can favor the efficient transferring of photo-carriers.

Based on the above analysis, the electronic property of g-C_3N_4 could be efficiently optimized *via* the in-situ introduction of C_{ring}. As shown in Fig. 6e, the rate determining step (RDS) of $2e^-$ ORR for HCN was located on the process of O_2 adsorption ($O_2 \rightarrow *O_2$) and the Gibbs free energy (ΔG) was 0.514 eV (Table S4). However, for CHCN, the reduction of *OOH (*$O_2 \rightarrow *OOH$) was the RDS during the $2e^-$ ORR process, but the ΔG was only 0.31 eV. Owning to the lower ΔG of the RDS for CHCN, the O_2 reduction to H_2O_2 performed on CHCN would be more efficient. Furthermore, the excellent electronic properties of CHCN can also greatly decrease the adsorption energy for *O_2 and *OOH (Fig. 6f), and the related models were illustrated in Fig. S16. Evidently, due to the abundant electrons transferring from the C_{ring} to g-C_3N_4, the O_2 and •OOH groups can be easily adsorbed on the surface of CHCN, compared to HCN. Therefore, the CHCN possessed *O_2 and *OOH adsorption energy of 3.14 and 3.45 eV, respectively, obviously lower than that of HCN (5.43 eV, 4.71 eV) (Table S5). In conclusion, with respect to HCN, the CHCN exhibited a higher efficiency of photocatalytic H_2O_2 generation in terms of ORR process.

4. Conclusion

In conclusion, we developed a highly active and stable tube-like g-C_3N_4 for photocatalytic H_2O_2 production through supramolecular self-assembly strategy, co-inducing by hydrogen and covalent bonds. This novel structural carbon nitride demonstrated excellent charge transfer/separation efficiency, owing to the emergence of the intrinsic driving force led by the in-plane C_{ring} of g-C_3N_4, and the photo-generated electrons could be easily transferred from the C_{ring} to the g-C_3N_4 (CHCN). Meanwhile, the hollow structure of the CHCN exhibited larger specific surface area, excellent electronic property, and more positive VB position, which were beneficial to the O_2 absorption/activation and ethanol/water oxidation to produce protons, respectively. As the proposed mechanism illustrated in Scheme 2, the optimized sample of CHCN-0.02 possesses high efficiency of the dominated route of one-step two-electron ORR, as well as efficient two-step single-electron ORR, where the maximum accumulation reached 1.58 mmol L^{-1} h^{-1}. Our work contributes to the developing design guidelines of promising metal-free g-C_3N_4-based catalysts for achieving efficient one/two-electron ORR in photocatalytic H_2O_2 production.

CRediT authorship contribution statement

Hao Luo: Methodology, Writing, Validation. **Tianshang Shan:** Software. **Jianwen Zhou:** Investigation. **Liulian Huang:** Resources. **Lihui Chen:** Resources. **Rongjian Sa:** Software. **Yusuke Yamauchi:** Editing, Validation. **Jungmok You:** Investigation. **Yusuke Asakura:** Editing. **Zhanhui Yuan:** Investigation. **He Xiao:** Conceptualization, Writing, Editing.

Declaration of Competing Interest

The authors declare the following financial interests/personal relationships which may be considered as potential competing interests: Yusuke Yamauchi's report was provided by University of Queensland. Yusuke Yamauchi reports a relationship with University of Queensland that includes: employment.

Data Availability

No data was used for the research described in the article.

Acknowledgments

Appendix A. Supporting information

Supplementary data associated with this article can be found in the online version at doi:10.1016/j.apcatb.2023.122933.

References

[1] L. Zhou, J. Feng, B. Qiu, Y. Zhou, J. Lei, M. Xing, L. Wang, Y. Zhou, Y. Liu, J. Zhang, Ultrathin g-C_3N_4 nanosheet with hierarchical pores and desirable energy band for highly efficient H_2O_2 production, Appl. Catal. B: Environ. 267 (2020), 118396.

[2] M. Melchionna, P. Fornasiero, M. Prato, The rise of hydrogen peroxide as the main product by metal-free catalysis in oxygen reductions, Adv. Mater. 31 (2019), 1802920.

[3] J. Zhang, L. Zheng, F. Wang, C. Chen, H. Wu, S.A.K. Leghari, M. Long, The critical role of furfural alcohol in photocatalytic H_2O_2 production on TiO_2, Appl. Catal. B: Environ. 269 (2020), 118770.

[4] S. Fukuzumi, Production of liquid solar fuels and their use in fuel cells, Joule 1 (2017) 689–738.

[5] J. Fu, Q. Xu, J. Low, C. Jiang, J. Yu, Ultrathin 2D/2D WO_3/g-C_3N_4 step-scheme H_2-production photocatalyst, Appl. Catal. B: Environ. 243 (2019) 556–565.

[6] R. Ma, L. Wang, H. Wang, Z. Liu, M. Xing, L. Zhu, X. Meng, F.-S. Xiao, Solid acids accelerate the photocatalytic hydrogen peroxide synthesis over a hybrid catalyst of titania nanotube with carbon dot, Appl. Catal. B: Environ. 244 (2019) 594–603.

[7] G.-h Moon, M. Fujitsuka, S. Kim, T. Majima, X. Wang, W. Choi, Eco-friendly photochemical production of H_2O_2 through O_2 reduction over carbon nitride frameworks incorporated with multiple heteroelements, ACS Catal. 7 (2017) 2886–2895.

[8] Y. Kondo, K. Honda, Y. Kuwahara, K. Mori, H. Kobayashi, H. Yamashita, Boosting photocatalytic hydrogen peroxide production from oxygen and water using a hafnium-based metal-organic framework with missing-linker defects and nickel single atoms, ACS Catal. 12 (2022) 14825–14835.

[9] Z. Teng, Q. Zhang, H. Yang, K. Kato, W. Yang, Y.-R. Lu, S. Liu, C. Wang, A. Yamakata, C. Su, B. Liu, T. Ohno, Atomically dispersed antimony on carbon nitride for the artificial photosynthesis of hydrogen peroxide, Nat. Catal. 4 (2021) 374–384.

[10] L. Yang, G. Dong, D.L. Jacobs, Y. Wang, L. Zang, C. Wang, Two-channel photocatalytic production of H_2O_2 over g-C_3N_4 nanosheets modified with perylene imides, J. Catal. 352 (2017) 274–281.

[11] J. Cao, H. Wang, Y. Zhao, Y. Liu, Q. Wu, H. Huang, M. Shao, Y. Liu, Z. Kang, Phosphorus-doped porous carbon nitride for efficient sole production of hydrogen peroxide via photocatalytic water splitting with a two-channel pathway, J. Mater. Chem. A 8 (2020) 3701–3707.

[12] C. Feng, L. Tang, Y. Deng, J. Wang, J. Luo, Y. Liu, X. Ouyang, H. Yang, J. Yu, J. Wang, Synthesis of leaf-vein-like g-C_3N_4 with tunable band structures and charge transfer properties for selective photocatalytic H_2O_2 evolution, Adv. Funct. Mater. 30 (2020), 2001922.

[13] W. Liu, C. Song, M. Kou, Y. Wang, Y. Deng, T. Shimada, L. Ye, Fabrication of ultra-thin g-C_3N_4 nanoplates for efficient visible-light photocatalytic H_2O_2 production via two-electron oxygen reduction, Chem. Eng. J. 425 (2021), 130615.

[14] C. Chu, W. Miao, Q. Li, D. Wang, Y. Liu, S. Mao, Highly efficient photocatalytic H_2O_2 production with cyano and SnO_2 co-modified g-C_3N_4, Chem. Eng. J. 428 (2022), 132531.

[15] L. Chen, C. Chen, Z. Yang, S. Li, C. Chu, B. Chen, Simultaneously tuning band structure and oxygen reduction pathway toward high-efficient photocatalytic hydrogen peroxide production using cyano-rich graphitic carbon nitride, Adv. Funct. Mater. 31 (2021), 2105731.

[16] H. Zhu, Q. Xue, G. Zhu, Y. Liu, X. Dou, X. Yuan, Decorating Pt@cyclodextrin nanoclusters on C_3N_4/MXene for boosting the photocatalytic H_2O_2 production, J. Mater. Chem. A 9 (2021) 6872–6880.

[17] W. Miao, Y. Liu, X. Chen, Y. Zhao, S. Mao, Tuning layered Fe-doped g-C_3N_4 structure through pyrolysis for enhanced Fenton and photo-Fenton activities, Carbon 159 (2020) 461–470.

[18] Q. He, B. Viengkeo, X. Zhao, Z. Qin, J. Zhang, X. Yu, Y. Hu, W. Huang, Y. Li, Multiscale structural engineering of carbon nitride for enhanced photocatalytic H_2O_2 production, Nano Res. (2021), https://doi.org/10.1007/s12274-021-3882-1.

[19] Y. Wang, P. Du, H. Pan, L. Fu, Y. Zhang, J. Chen, Y. Du, N. Tang, G. Liu, Increasing solar absorption of atomically thin 2D carbon nitride sheets for enhanced visible-light photocatalysis, Adv. Mater. 31 (2019), 1807540.

[20] C. Xiao, L. Zhang, K. Wang, H. Wang, Y. Zhou, W. Wang, A new approach to enhance photocatalytic nitrogen fixation performance via phosphate-bridge: a case study of SiW_{12}/K-C_3N_4, Appl. Catal. B: Environ. 239 (2018) 260–267.

[21] S. Cao, B. Fan, Y. Feng, H. Chen, F. Jiang, X. Wang, Sulfur-doped g-C_3N_4 nanosheets with carbon vacancies: general synthesis and improved activity for simulated solar-light photocatalytic nitrogen fixation, Chem. Eng. J. 353 (2018) 147–156.

[22] J. Fu, J. Yu, C. Jiang, C. Bei, g-C_3N_4-Based heterostructured photocatalysts, Adv. Energy Mater. 8 (2018), 1701503.

[23] H. Ou, P. Yang, L. Lin, M. Anpo, X. Wang, Carbon nitride aerogels for the photoredox conversion of water, Angew. Chem. Int. Ed. 56 (2017) 10905–10910.

[24] L. Jiang, X. Yuan, Y. Pan, J. Liang, G. Zeng, Z. Wu, H. Wang, Doping of graphitic carbon nitride for photocatalysis: a reveiw, Appl. Catal. B: Environ. 217 (2017) 388–406.

[25] X. Yang, J. Ma, S. Sun, Z. Liu, R. Sun, K/O co-doping and introduction of cyano groups in polymeric carbon nitride towards efficient simultaneous solar photocatalytic water splitting and biorefineries, Green. Chem. 24 (2022) 2104–2113.

[26] Z. Wei, M. Liu, Z. Zhang, W. Yao, H. Tan, Y. Zhu, Efficient visible-light-driven selective oxygen reduction to hydrogen peroxide by oxygen-enriched graphitic carbon nitride polymers, Energy Environ. Sci. 11 (2018) 2581–2589.

[27] R. Du, K. Xiao, B. Li, X. Han, C. Zhang, X. Wang, Y. Zuo, P. Guardia, J. Li, J. Chen, J. Arbiol, A. Cabot, Controlled oxygen doping in highly dispersed Ni-loaded g-C_3N_4 nanotubes for efficient photocatalytic H_2O_2 production, Chem. Eng. J. 441 (2022), 135999.

[28] Y.-Y. Li, B.-X. Zhou, H.-W. Zhang, T. Huang, Y.-M. Wang, W.-Q. Huang, W. Hu, A. Pan, X. Fan, G.-F. Huang, A host-guest self-assembly strategy to enhance π-electron densities in ultrathin porous carbon nitride nanocages toward highly efficient hydrogen evolution, Chem. Eng. J. 430 (2022), 132880.

[29] H. Fattahimoghaddam, T. Mahvelati-Shamsabadi, B.-K. Lee, Enhancement in photocatalytic H_2O_2 production over g-C_3N_4 nanostructures: acollaborative approach of nitrogen deficiency and supramolecular precursors, ACS Sustain. Chem. Eng. 9 (2021) 4520–4530.

[30] K. Liu, J. Ma, X. Yang, Z. Liu, X. Li, J. Zhang, R. Cui, R. Sun, Phosphorus/oxygen co-doping in hollow-tube-shaped carbon nitride for efficient simultaneous visible-light-driven water splitting and biorefinery, Chem. Eng. J. 437 (2022), 135232.

[31] Z. Mo, J. Di, P. Yan, C. Lv, X. Zhu, D. Liu, Y. Song, C. Liu, Q. Yu, H. Li, Y. Lei, H. Xu, Q. Yan, An all-organic D-A System for visible-light-driven overall water splitting, Small 16 (2020), 2003914.

[32] H. Ou, S. Ning, P. Zhu, S. Chen, A. Han, Q. Kang, Z. Hu, J. Ye, D. Wang, Y. Li, Carbon nitride photocatalysts with integrated oxidation and reduction atomic active centers for improved CO_2 conversion, Angew. Chem. Int. Ed. 61 (2022), e202206579.

[33] B. Li, Q. Fang, Y. Si, T. Huang, W.-Q. Huang, W. Hu, A. Pan, X. Fan, G.-F. Huang, Ultra-thin tubular graphitic carbon nitride-carbon dot lateral heterostructures: one-step synthesis and highly efficient catalytic hydrogen generation, Chem. Eng. J. 397 (2020), 125074.

[34] B.-X. Zhou, S.-S. Ding, B.-J. Zhang, L. Xu, R.-S. Chen, L. Luo, W.-Q. Huang, Z. Xie, A. Pan, G.-F. Huang, Dimensional transformation and morphological control of graphitic carbon nitride from water-based supramolecular assembly for photocatalytic hydrogen evolution: from 3D to 2D and 1D nanostructures, Appl. Catal. B: Environ. 254 (2019) 321–328.

[35] W. Che, W. Cheng, T. Yao, F. Tang, W. Liu, H. Su, Y. Huang, Q. Liu, J. Liu, F. Hu, Z. Pan, Z. Sun, S. Wei, Fast Photoelectron transfer in (Cring)–C_3N_4 Plane heterostructural nanosheets for overall water splitting, J. Am. Chem. Soc. 139 (2017) 3021–3026.

[36] Shen Zhao, Tao Guo, Xia Li, Tongguang Xu, Bo Yang, Xu Zhao, Carbon nanotubes covalent combined with graphitic carbon nitride for photocatalytic hydrogen peroxide production under visible light, Appl. Catal. B. Environ. Int. J. Devoted Catal. Sci. Appl. 224 (2018) 725–732.

[37] A.M. Zoghi, S. Allahyari, Multifunctional magnetic C_3N_4-rGO adsorbent with high hydrophobicity and simulated solar light-driven photocatalytic activity for oil spill removal, Sol. Energy 237 (2022) 320–332.

[38] L. Zhou, J. Lei, F. Wang, L. Wang, M.R. Hoffmann, Y. Liu, S.-I. In, J. Zhang, Carbon nitride nanotubes with in situ grafted hydroxyl groups for highly efficient spontaneous H_2O_2 production, Appl. Catal. B: Environ. 288 (2021), 119993.

[39] Y. Wu, X. Mao, M. Zhang, X. Zhao, R. Xue, S. Di, W. Huang, L. Wang, Y. Li, Y. Li, 2D molecular sheets of hydrogen-bonded organic frameworks for ultrastable sodium-Ion storage, Adv. Mater. 33 (2021), 2106079.

[40] B. Wang, X.-L. Lv, J. Lv, L. Ma, R.-B. Lin, H. Cui, J. Zhang, Z. Zhang, S. Xiang, B. Chen, A novel mesoporous hydrogen-bonded organic framework with high porosity and stability, Chem. Commun. 56 (2020) 66–69.

[41] B. Yu, S. Geng, H. Wang, W. Zhou, Z. Zhang, B. Chen, J. Jiang, A solid transformation into carboxyl dimers based on a robust hydrogen-bonded organic framework for propyne/propylene separation, Angew. Chem. Int. Ed. 60 (2021) 25942–25948.

[42] B. Yu, T. Meng, X. Ding, X. Liu, H. Wang, B. Chen, T. Zheng, W. Li, Q. Zeng, J. Jiang, Hydrogen-bonded organic framework ultrathin nanosheets for efficient visible-light photocatalytic CO_2 reduction, Angew. Chem. Int. Ed. 61 (2022), e202211482.

[43] M. Vicent-Morales, M. Esteve-Rochina, J. Calbo, E. Ortí, I.J. Vitórica-Yrezábal, G. Mínguez, Espallargas, Semiconductor porous hydrogen-bonded organic frameworks based on tetrathiafulvalene derivatives, J. Am. Chem. Soc. 144 (2022) 9074–9082.

[44] X. Zhang, L. Li, J.-X. Wang, H.-M. Wen, R. Krishna, H. Wu, W. Zhou, Z.-N. Chen, B. Li, G. Qian, B. Chen, Selective ethane/ethylene separation in a robust microporous hydrogen-bonded organic framework, J. Am. Chem. Soc. 142 (2020) 633–640.

[45] A. Khalid, A. Ibrahim, O.C.S. Al-Hamouz, T. Laoui, A. Benamor, M.A. Atieh, Fabrication of polysulfone nanocomposite membranes with silver-doped carbon nanotubes and their antifouling performance, J. Appl. Polym. Sci. 134 (2017) 15.

[46] Y. Shan, Y. Guo, Y. Wang, X. Du, L. Chen, Nanocellulose-derived carbon/g-C_3N_4 heterojunction with a hybrid electron transfer pathway for highly photocatalytic hydrogen peroxide production, J. Colloid Interface Sci. 599 (2021) 507–518.

[47] Y. Zheng, Y. Luo, Q. Ruan, S. Wang, J. Yu, X. Guo, W. Zhang, H. Xie, Z. Zhang, Y. Huang, Plasma-induced hierarchical amorphous carbon nitride nanostructure with two N_2C-site vacancies for photocatalytic H_2O_2 production, Appl. Catal. B: Environ. 311 (2022) 121372.

[48] B. Liu, J. Du, G. Ke, B. Jia, Y. Huang, H. He, Y. Zhou, Z. Zou, Boosting O_2 reduction and H_2O dehydrogenation kinetics: surface N-hydroxymethylation of g-C_3N_4 photocatalysts forthe efficient production of H_2O_2, Adv. Funct. Mater. 32 (2021), 2111125.

[49] Z. Mo, H. Xu, Z. Chen, X. She, Y. Song, J. Wu, P. Yan, L. Xu, Y. Lei, S. Yuan, H. Li, Self-assembled synthesis of defect-engineered graphitic carbon nitride nanotubes for efficient conversion of solar energy, Appl. Catal. B: Environ. 225 (2018) 154–161.

[50] L. Li, M. Shalom, Y. Zhao, J. Barrio, M. Antonietti, Surface polycondensation as an effective tool to activate organic crystals: from "boxed" semiconductors for water oxidation to 1D carbon nanotubes, J. Mater. Chem. A 5 (2017) 18502–18508.

[51] B. Wu, L. Zhang, B. Jiang, Q. Li, C. Tian, Y. Xie, W. Li, H. Fu, Ultrathin porous carbon nitride bundles with an adjustable energy band structure toward simultaneous solar photocatalytic water splitting and selective phenylcarbinol oxidation, Angew. Chem. Int. Ed. 60 (2021), 4951-4951.

[52] N. Keshavarzi, S. Cao, M. Antonietti, A new conducting polymer with exceptional visible-Light photocatalytic activity derived from barbituric acid polycondensation, Adv. Mater. 32 (2020), 1907702.

[53] M. Luo, Q. Yang, K. Liu, H. Cao, H. Yan, Boosting photocatalytic H_2 evolution on g-C_3N_4 by modifying covalent organic frameworks (COFs), Chem. Commun. 55 (2019) 5829–5832.

[54] J.-X. Wu, P.P. Bag, Y.-T. Xu, L. Gong, C.-T. He, X.-M. Chen, J.-P. Zhang, Graphene-like hydrogen-bonded melamine–cyanuric acid supramolecular nanosheets as pseudo-porous catalyst support, Adv. Mater. 33 (2021), 2007368.

[55] X. Wang, K. Maeda, A. Thomas, K. Takanabe, G. Xin, J.M. Carlsson, K. Domen, M. Antonietti, A metal-free polymeric photocatalyst for hydrogen production from water under visible light, Nat. Mater. 8 (2009) 76–80.

[56] J. Yan, M.T.F. Rodrigues, Z. Song, H. Li, H. Xu, H. Liu, J. Wu, Y. Xu, Y. Song, Y. Liu, Hydrogels: reversible formation of g-C_3N_4 3D hydrogels through ionic liquid activation: gelation behavior and room-temperature gas-sensing properties, Adv. Funct. Mater. 27 (2017) 1700651–1700653.

[57] K. Chen, D. Xue, Water-soluble inorganic salt with ultrahigh specific capacitance: $Ce(NO_3)_3$ can be designed as excellent pseudocapacitor electrode, J. Colloid Interface Sci. 416 (2014) 172–176.

[58] J. Xu, H. Wang, C. Zhang, X. Yang, S. Cao, J. Yu, M. Shalom, From Millimeter to subnanometer: vapor–solid deposition of carbon nitride hierarchical

[59] nanostructures directed by supramolecular assembly, Angew. Chem. Int. Ed. 56 (2017) 8426–8430.

[59] S. Guo, Y. Tang, Y. Xie, C. Tian, Q. Feng, W. Zhou, B. Jiang, P-doped tubular g-C_3N_4 with surface carbon defects: universal synthesis and enhanced visible-light photocatalytic hydrogen production, Appl. Catal. B: Environ. 218 (2017) 664–671.

[60] Y. Wang, X. Liu, J. Liu, B. Han, X. Hu, F. Yang, Z. Xu, Y. Li, S. Jia, Z. Li, Y. Zhao, Carbon quantum dot implanted graphite carbon nitride nanotubes: excellent charge separation and enhanced photocatalytic hydrogen evolution, Angew. Chem. Int. Ed. 57 (2018) 5765–5771.

[61] Y. Yu, W. Yan, X. Wang, P. Li, W. Gao, H. Zou, S. Wu, K. Ding, Surface engineering for extremely enhanced charge separation and photocatalytic hydrogen evolution on g-C_3N_4, Adv. Mater. 30 (2018), 1705060.

[62] Y. Zhang, J. Gao, Z. Chen, A solid-state chemical reduction approach to synthesize graphitic carbon nitride with tunable nitrogen defects for efficient visible-light photocatalytic hydrogen evolution, J. Colloid Interface Sci. 535 (2019) 331–340.

[63] K. Li, M. Sun, W.-D. Zhang, Polycyclic aromatic compounds-modified graphitic carbon nitride for efficient visible-light-driven hydrogen evolution, Carbon 134 (2018) 134–144.

[64] K.-Q. Lu, Y. Chen, X. Xin, Y.-J. Xu, Rational utilization of highly conductive, commercial elicarb graphene to advance the graphene-semiconductor composite photocatalysis, Appl. Catal. B: Environ. 224 (2018) 424–432.

[65] M. Wu, Y. Wang, Z. Wei, L. Wang, M. Zhuo, J. Zhang, X. Han, J. Ma, Ternary doped porous carbon nanofibers with excellent ORR and OER performance for zinc–air batteries, J. Mater. Chem. A 6 (2018) 10918–10925.

[66] H. Yu, L. Shang, T. Bian, R. Shi, G.I.N. Waterhouse, Y. Zhao, C. Zhou, L.-Z. Wu, C.-H. Tung, T. Zhang, Nitrogen-doped porous carbon nanosheets Templated from g-C_3N_4 as metal-free electrocatalysts for efficient oxygen reduction reaction, Adv. Mater. 28 (2016) 5080–5086.

[67] Y. Dong, Q. Wang, H. Wu, Y. Chen, C.-H. Lu, Y. Chi, H.-H. Yang, Graphitic carbon nitride materials: sensing, imaging and therapy, Small 12 (2016) 5376–5393.

[68] I. Krivtsov, D. Mitoraj, C. Adler, M. Ilkaeva, M. Sardo, L. Mafra, C. Neumann, A. Turchanin, C. Li, B. Dietzek, R. Leiter, J. Biskupek, U. Kaiser, C. Im, B. Kirchhoff, T. Jacob, R. Beranek, Water-soluble polymeric carbon nitride colloidal nanoparticles for highly selective quasi-homogeneous photocatalysis, Angew. Chem. Int. Ed. 59 (2020) 487–495.

[69] T. Song, G. Zeng, P. Zhang, T. Wang, S. Huang, H. Zeng, Ultrathin carbon nitride with atomic-level intraplane implantation of graphited carbon ring domain for superior photocatalytic activity in the visible/near-infrared region, ACS Sustain. Chem. Eng. 7 (2019) 1239–1249.

[70] W. Xing, W. Tu, Z. Han, Y. Hu, Q. Meng, G. Chen, Template-induced high-crystalline g-C_3N_4 nanosheets for enhanced photocatalytic H_2 evolution, ACS Energy Lett. 3 (2018) 514–519.

[71] W. Ho, Z. Zhang, W. Lin, S. Huang, X. Zhang, X. Wang, Y. Huang, Copolymerization with 2,4,6-triaminopyrimidine for the rolling-up the layer structure, tunable electronic properties, and photocatalysis of g-C_3N_4, ACS Appl. Mater. Interfaces 7 (2015) 5497–5505.

[72] S. Yang, Y. Gong, J. Zhang, L. Zhan, L. Ma, Z. Fang, R. Vajtai, X. Wang, P. M. Ajayan, Exfoliated graphitic carbon nitride nanosheets as efficient catalysts for hydrogen evolution under visible light, Adv. Mater. 25 (2013) 2452–2456.

[73] J. Li, F. Wei, Z. Xiu, X. Han, Direct Z-scheme charge transfer of Bi_2WO_6/$InVO_4$ interface for efficient photocatalytic CO_2 reduction, Chem. Eng. J. 446 (2022), 137129.

[74] L. Wang, J. Zhang, Y. Zhang, H. Yu, Y. Qu, J. Yu, Inorganic metal-oxide photocatalyst for H_2O_2 production, Small 18 (2022), 2104561.

[75] C. Chu, Q. Li, W. Miao, H. Qin, X. Liu, D. Yao, S. Mao, Photocatalytic H_2O_2 production in a cyclodextrin-pyrimidine polymer in a wide pH range without electron donor or oxygen aeration, Appl. Catal. B: Environ. 314 (2022) 121485.

[76] Z. Zhu, H. Pan, M. Murugananthan, J. Gong, Y. Zhang, Visible light-driven photocatalytically active g-C_3N_4 material for enhanced generation of H_2O_2, Appl. Catal. B: Environ. 232 (2018) 19–25.

[77] J. Luo, Y. Liu, C. Fan, L. Tang, S. Yang, M. Liu, M. Wang, C. Feng, X. Ouyang, L. Wang, L. Xu, J. Wang, M. Yan, Direct attack and indirect transfer mechanisms dominated by reactive oxygen species for photocatalytic H_2O_2 production on g-C_3N_4 possessing nitrogen vacancies, ACS Catal. 11 (2021) 11440–11450.

[78] P. Sun, Z. Mo, H. Chen, Y. Song, J. Liu, W. Yin, H. Dai, Z. Chen, H. Li, H. Xu, Highly efficient photosynthesis of H_2O_2 via two-channel pathway photocatalytic water splitting, Inorg. Chem. Front. 9 (2022) 1701–1707.

[79] J. Yang, J. Jing, Y. Zhu, A full-spectrum porphyrin-fullerene D-A supramolecular photocatalyst with giant built-in electric field for efficient hydrogen production, Adv. Mater. 33 (2021), 2101026.

[80] K. Wang, C.-J. Zheng, W. Liu, K. Liang, Y.-Z. Shi, S.-L. Tao, C.-S. Lee, X.-M. Ou, X.-H. Zhang, Avoiding energy loss on TADF emitters: controlling the dual conformations of D-A structure molecules based on the pseudoplanar segments, Adv. Mater. 29 (2017), 1701476.

[81] M. Wolf, J.I.T. Costa, M.B. Minameyer, T. Drewello, A.C. Tome, D.M. Guldi, Efficient low driving force charge separation in an electron deficient Zn-porphyrin-fullerene donor-acceptor conjugate, J. Phys. Chem. C 123 (2019) 28093–28099.